



1 **A new merged dataset for analyzing clouds, precipitation**
2 **and atmospheric parameters based on ERA5 reanalysis**
3 **data and the measurements of TRMM PR and VIRS**

4 Lili Sun¹, Yunfei Fu¹

5 ¹School of Earth and Space Sciences, University of Science and Technology of China, Hefei, 230026,
6 China

7 *Correspondence to: Yunfei Fu (fyf@ustc.edu.cn)*

8 **Abstract.** Clouds and precipitation have vital roles in the global hydrological cycle and the radiation
9 budget of the atmosphere–Earth system and are closely related to both the regional and global climate.
10 Changes in the status of the atmosphere inside clouds and precipitation systems are also important, but
11 the use of multi-source datasets is hampered by their different spatial and temporal resolutions. We
12 merged the precipitation parameters measured by the Tropical Rainfall Measuring Mission (TRMM)
13 Precipitation Radar (PR) with the multi-channel cloud-top radiance measured by the Visible and Infrared
14 Scanner (VIRS) and atmospheric parameters in the ERA5 reanalysis dataset. The merging of pixels
15 between the precipitation parameters and multi-channel cloud-top radiance was shown to be reasonable.
16 The 1B01-2A25 dataset of pixel-merged data (1B01-2A25-PMD) contains cloud parameters for each PR
17 pixel. The 1B01-2A25 gridded dataset (1B01-2A25-GD) was merged spatially with the ERA5 reanalysis
18 data. The statistical results indicate that gridding has no unacceptable influence on the parameters in the
19 1B01-2A25-PMD. In one orbit, the difference in the mean value of the near-surface rain rate and the
20 signals measured by the VIRS was no more than 0.87 and the standard deviation was no more than 2.38.
21 The 1B01-2A25-GD and ERA5 datasets were spatiotemporally collocated to establish the merged 1B01-
22 2A25 gridded dataset (M-1B01-2A25-GD). Three case studies of typical cloud and precipitation events
23 were analyzed to illustrate the practical use of the M-1B01-2A25-GD. This new merged gridded dataset
24 can be used to study clouds and precipitation systems and provides a perfect opportunity for multi-source
25 data analysis and model simulations. The data which were used in this paper are freely available at
26 <http://doi.org/10.5281/zenodo.4458868> (Sun and Fu, 2021).

27 **1 Introduction**



28 Clouds and precipitation are the result of interactions among several different atmospheric parameters.
29 They have a crucial role in global hydrological and energy cycles which can be used to represent changes
30 in the Earth's weather and climate (Hartmann and Short, 1980; Liou, 1986; Wetherald and Manabe, 1988;
31 Baker, 1997; Houze, 1997; Roscow et al., 1999; Oki and Kanae, 2006; Lau and Wu, 2010; Fu and Zhang,
32 2018). More than two-thirds of all precipitation falls in the tropics and subtropics. The atmosphere
33 obtains energy from the release of the latent heat of condensation during precipitation and this is one of
34 the main drivers of atmospheric circulation at low latitudes. Precipitating clouds also influence the
35 Earth's radiation budget (Fu et al., 2006; Sassen et al., 2009; Kienast-Sjögren et al., 2016; Fu and Zhang,
36 2018; Gao et al., 2018). Atmospheric parameters (e.g., the temperature, pressure and wind fields) can be
37 used to demonstrate changes in atmospheric status and the development of cloud and precipitation
38 systems (Wang et al., 2015; Zheng et al., 2015; Pan and Fu, 2015; Xia and Fu, 2016; Wang et al., 2017).
39 Analysis of the complex distribution of clouds and precipitation, especially their 3D structures, helps to
40 require a detailed understanding of the microphysical processes and thermodynamic structure of clouds.
41 The horizontal structure represents the extent of the system, whereas the thermodynamic structure and
42 microphysical processes inside clouds during the phase transition of water can be represented by the
43 vertical structure (Houze, 1981; Szoke et al., 1986; Hobbs, 1991; Zipser and Lutz, 1994; Yuter and Houze,
44 1995; Liu and Fu, 2001; Luo et al., 2009). A comprehensive understanding of the 3D structure of
45 precipitation and clouds will improve precipitation retrieval algorithms and model simulations (Wilheit
46 et al., 1977; Petty, 1994; Kummerow et al., 1996; Olson et al., 1996; Iguchi et al., 2000; Tustison et al.,
47 2002; Min et al., 2013).

48 Satellite remote sensing technology has developed rapidly in recent years. The first space-borne active
49 radar is the Precipitation Radar (PR) onboard the Tropical Rainfall Measurement Mission (TRMM)
50 (Kummerow et al., 1998; Kummerow et al., 2000; Kozu et al., 2001). The main aim of the TRMM is the
51 effective observation of precipitation and energy exchange in tropical and subtropical regions. The
52 unique instruments onboard the satellite provide an excellent opportunity to study the 3D structure of
53 precipitation (Nesbitt et al., 1999; Schumacher and Houze, 2003; Durden et al., 2003; Li and Fu, 2005;
54 Liu and Zipser, 2009), whereas the Visible and Infrared Scanner (VIRS) provides characteristics of cloud
55 parameters near the cloud-top (Liu and Fu, 2010; Fu, 2014; Yang et al., 2014; Chen and Fu, 2017).
56 Many studies of the 3D structure of clouds and precipitation have been based on TRMM measurements



57 (Fu and Liu, 2001; Lu et al., 2016; Wang and Fu, 2017; Luo et al., 2020). Chen and Fu (2015) focused
58 on the characteristics of precipitation and thermal infrared signals of clouds in typhoon and non-typhoon
59 precipitation in eastern Asia by analyzing merged data between the PR and the VIRS pixels. Results
60 showed that the most intense typhoon precipitation occurred on the ocean surface in eastern Asia. Non-
61 typhoon precipitation was the main type of precipitation in the rainy season, but typhoon precipitation
62 made the largest contributed to the total amount of precipitation. Yang et al. (2014) statistically analyzed
63 10-year data from the TRMM PR and VIRS and found that the cloud height and thickness of anvil clouds
64 over land were always greater than those over the sea surface, and anvil clouds had a greater optical
65 thickness over the land surface and more small ice particles.

66 Liu and Fu (2001) classified tropical precipitation into two main types (deep convective and stratiform)
67 using the main component method. The mean rain rate profiles of deep convective rain had four layers,
68 whereas stratiform precipitation had only three. Differences in the slopes of the mean profiles can be
69 used to illustrate the microphysical processes at different vertical structure of the rainfall. Liu and Fu
70 (2007) compared rain rate profiles from the Tibetan Plateau, eastern Asia and the tropics. It was found
71 that there was little stratiform precipitation on the Tibetan Plateau, but deep weak convective
72 precipitation was frequently detected in this region. The slope of the mean deep weak convective profile
73 was greater than that for convective precipitation, which meant that more latent heat was released to heat
74 the middle and upper atmosphere. Fu et al. (2008) found that the tops of precipitating clouds were about
75 4–6 km higher than that in the surrounding area. The difference in the clouds tops height led to a tower-
76 like structure over the Tibetan Plateau, which can heat the upper troposphere more easily.

77 Recent researchs has investigated the status of the atmosphere in clouds and precipitation systems (Wang
78 and Fu, 2017; Li et al., 2018). In addition to observations from surface meteorological stations,
79 atmospheric parameters can be obtained from sounding balloons, sensors onboard planes and model
80 simulations. Because of the uneven distribution of ground meteorological stations, the unpredictable
81 routes of sounding balloons and the limited detection area of planes. We therefore analyzed the
82 characteristics and distribution of atmospheric parameters inside clouds and precipitation systems using
83 the ERA5 reanalysis dataset.

84 It is impossible to obtain simultaneous and comprehensive information using a single detection method
85 or dataset as a result of the different ways of obtaining the cloud, precipitation and atmospheric



86 parameters. The optimum choice to overcome this problem is to combine multiple remote sensing
87 measurements and multi-source datasets (Fu et al., 2013; Chen and Fu, 2017). Hawkins et al. (2008)
88 combined multiple source datasets, including satellite cloud imagery captured by cloud profile radar and
89 stationary satellites, observations from experimental planes and model simulations. The merged data can
90 be used to determine the vertical structure of precipitating clouds and the atmospheric parameters in
91 typhoon, frontal and thermal convective precipitation systems.

92 VIRS pixels can be merged onto PR pixels in a similar way to verify precipitating clouds. The results of
93 this type of merger have shown that the reflectivity in the visible channel near the precipitating cloud-
94 top is bigger than 0.5 in the intertropical convergence zone, convergence zone of the southern hemisphere,
95 the monsoon region of Asia, the tropical regions of Africa, North America and South America. The
96 reflectivity on land is greater than that on the sea surface (Fu et al., 2011). Liu and Fu (2010) verified
97 precipitating clouds from several typhoon and frontal precipitation events in eastern China based on the
98 same merged dataset. Precipitating clouds cannot be classified precisely by relying on only the thermal
99 infrared brightness temperature and other parameters are needed to improve the accuracy, such as the
100 ratio between the signals in the visible and near infrared channels.

101 The various temporal and spatial resolutions of different datasets can cause problems and it is better to
102 merge data from multiple instruments onboard the same satellite, such as the TRMM. The ERA5
103 reanalysis dataset has a suitable temporospatial resolution for merging with the TRMM data to
104 supplement the atmospheric parameters. This new merged dataset includes comprehensive parameters
105 that can be used to analyze the features of the precipitation and clouds systems.

106 We merged TRMM PR and VIRS measurements with the ERA5 reanalysis data at the same
107 spatiotemporal resolution to establish a new dataset of precipitation, cloud and atmospheric parameters.
108 Section 2 describes the data and merging methods. Section 3 presents the main results about the influence
109 of the merger on the original data during the merging process and the practical applications of the new
110 merged dataset. Section 4 discusses the advantages of the dataset and future work in the progress. Access
111 to the dataset is introduced in Section 5 and conclusions are presented in Section 6.



112 **2 Data and methods**

113 **2.1 Tropical Rainfall Measurement Mission**

114 The TRMM was launched in November 1997 as a joint mission between the US National Aeronautics
115 and Space Administration (NASA) and the Japan Aerospace Exploration Agency (JAXA). The
116 objectives of the TRMM are to obtain satellite measurements of rainfall and energy exchange in tropical
117 and subtropical regions (https://trmm.gsfc.nasa.gov/overview_dir/background.html). The TRMM is a
118 non-solar synchronous polar orbiting satellite in a 350 km (402 km after an orbital boost on 7 August
119 2001) circular orbit with an inclination angle of 35°. The TRMM observes a specific location between
120 38° S and 38° N every 45 days. One complete scan of the orbit takes about 96 minutes, so there are 16
121 orbits in one day (Simpson et al., 1996; Kummerow et al., 1998).

122 **2.2 PR and 2A25 dataset**

123 The PR was the first space-borne precipitation radar onboard the TRMM. It is a 128-element active
124 phased array system operating at 13.8 GHz (Kozu et al., 2001). The PR antenna scans in the cross-track
125 direction over 17° in a 215 km (220 km after the orbital boost) swath width. There are 49 pixels in each
126 scan line. The PR measures the spatial distribution of the intensity of precipitation from mean sea-level
127 to 20 km (80 layers in total) and has a horizontal resolution of 4.5 km at nadir (5 km after the orbital
128 boost). The vertical resolution of the PR is 0.25 km.

129 The 2A25 data produced by NASA Goddard Space Flight Center is the second-level data product of the
130 TRMM PR. The dataset includes the scan time, geolocation information, rain type, 3D rain rate and so
131 on. The TRMM PR algorithm classifies the type of rain into convective, stratiform and “other” (Awaka
132 et al., 1997; Hayasaka et al., 1998).

133 **2.3 VIRS and 1B01 datasets**

134 The VIRS antenna scans in the cross-track direction over 45° in a 720 km (833 km after the orbital boost)
135 swath width. There are 261 pixels in each scan line and the horizontal resolution is 2.2 km at nadir (2.4
136 km after the orbital boost). The VIRS receives upward radiation at five wavelengths ranging from the
137 visible to the far infrared: 0.63 μm (CH1), 1.6 μm (CH2), 3.7 μm (CH3), 10.8 μm (CH4) and 12.0 μm
138 (CH5).

139 The 1B01 dataset is the first-level data product of the VIRS. The 1B01 data include the reflectivity in



140 CH1 and CH2 (RF1 and RF2) and the infrared radiation brightness temperature ($T_{B_{3.7}}$, $T_{B_{10.8}}$ and $T_{B_{12.0}}$)
141 in CH3, CH4 and CH5, which are calibrated from the spectral signals measures by the VIRS.

142 **2.4 ERA5 reanalysis dataset**

143 The ERA5 reanalysis dataset is the fifth (latest) generation of global atmospheric reanalysis datasets
144 produced by the European Centre for Medium-Range Weather Forecasts. The ERA5 dataset is based on
145 the Integrated Forecasting System Cy41r2 model and assimilates more model simulation outputs and
146 observational results. The ERA5 dataset is superior to previous versions in terms of its hourly output,
147 finer spatial resolution (0.25°) and abundant parameters (Zhao et al., 2019; Hersbach et al., 2020). We
148 used the hourly atmospheric parameters (divergence, geopotential height, specific humidity, wind field,
149 vertical velocity and temperature) on pressure levels for 32 layers from 1000 to 10 hPa. All the pressure
150 layers are used during the data merging, except the uppermost pressure layers from 1 to 7 hPa, which are
151 rarely used in studies.

152 **2.5 2A25 and 1B01 merged data**

153 The characteristics of precipitation and clouds are shown by identifying precipitating clouds from the
154 PR and detecting radiance near the top of the cloud by the VIRS (Liu and Fu, 2010; Fu et al., 2011;
155 Chen et al., 2018). The 2A25 and 1B01 data products (derived from the TRMM PR and VIRS,
156 respectively) can be collocated to establish a merged dataset to provide comprehensive information
157 about precipitation and clouds systems. The feasibility of data merging depends largely on the sensor
158 settings, such as the temporal sampling rate, the synchronism of detection and the spatial resolution.
159 The PR and the VIRS are both the main sensors onboard the TRMM. Despite the difference in spatial
160 resolution between 1B01 and 2A25, the time lag between detections of the same target is less than 1
161 minute. The similar cross-track scanning modes make it reasonable to consider that the PR and VIRS
162 are roughly synchronous in their detection area. It is therefore feasible to combine these two orbit-level
163 data products. Spatial merging is the only process that needs to be taken into account because of the
164 quasi-synchronicity between the TRMM PR and VIRS.
165 On account of the diverse orbital swath widths and spatial resolutions, the horizontal resolution of the
166 1B01 is decreased to match that of the 2A25 so that data merging can be easily achieved. The VIRS
167 pixels are merged onto the PR pixels through a weight-averaged method. The spectral signals are



168 calculated near the PR pixel and there are usually about seven VIRS pixels near one PR pixel (Fu et al.,
169 2011). The primary data of the 1B01 include the reflectivity at CH1 and CH2 (RF1 and RF2), the
170 equivalent brightness temperature of a black body at CH3, CH4 and CH5 ($T_{B3.7}$, $T_{B10.8}$ and $T_{B12.0}$), the
171 instantaneous near-surface rain rate and the vertical structure of precipitation in 2A25. All the VIRS
172 signals are within the resolution of the PR pixel which can be used to study the characteristics of
173 precipitating clouds. The 1B01-2A25 pixel-merged data (1B01-2A25-PMD) are then established (Liu
174 and Fu, 2010; Chen and Fu, 2015; Chen and Fu, 2017).

175 **2.6 Gridding of the 1B01-2A25-PMD**

176 Because the 1B01-2A25-PMD contains orbit-level data, data gridding is necessary to merge these data
177 with the ERA5 data. The 1B01-2A25-PMD is gridded between 40° S and 40° N and the spatial
178 resolution is 0.25°, in agreement with the resolution of the ERA5 data. Taking the near-surface rain rate
179 as an example, we first sum the near-surface rain rate of the pixels in the same grid and then counting
180 the number of precipitating pixels in one grid and dividing the total rain rate by the total number of
181 precipitating pixels to obtain the near-surface rain rate of one grid. The grid-level dataset, namely, the
182 1B01-2A25 gridded data (1B01-2A25-GD) is calculated in the same way. The dataset includes the
183 gridded spectral signals measured by the VIRS in each PR pixel. The precipitation is classified into
184 three types: total precipitation, convective precipitation, and stratiform precipitation. The PR is a Ku-
185 band radar with a working frequency of 13.8 GHz and a wavelength of 2.2 cm. The sensitivity of the
186 PR is 16 dBZ and the minimum rain rate it can detect is about 0.4 mm h⁻¹. Only pixels with a near-
187 surface rain rate greater than 0.4 mm h⁻¹ are calculated.

188 **2.7 Merging the ERA5 and 1B01-2A25-GD**

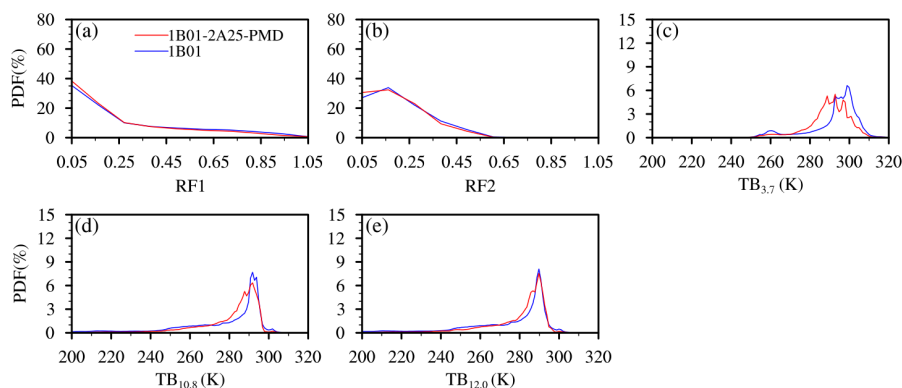
189 We merged the ERA5 data onto the 1B01-2A25-GD grid to explore the atmospheric status of the
190 precipitation and clouds systems measured by the sensors onboard the TRMM. The ERA5 dataset has
191 hourly outputs and the ERA5 parameters were therefore interpolated according to the grid times in the
192 1B01-2A25-GD. The geolocation of the ERA5 grid was selected to match that of the 1B01-2A25-GD.
193 The merged 1B01-2A25 gridded dataset (M-1B01-2A25-GD) was therefore obtained, which includes
194 geolocation information, the time of the grid and parameters for precipitation, clouds and the
195 atmosphere.



196 **3 Results**

197 **3.1 Evaluation of the 1B01-2A25-PMD**

198 The horizontal resolution of the 1B01 is decreased in the 1B01-2A25-PMD as a result of merging onto
199 the PR pixels. The detection field of the merged data is narrower than that in the 1B01 and is about the
200 same as the swath width of the PR. The influence on the original data in 1B01 after merging is
201 presented based on comparisons between the probability distribution functions (PDFs). Taking an
202 arbitrary orbit for example, orbit 37362 on 5 June 2004. Comparisons are made between the signals in
203 five spectral channels in the 1B01 and 1B01-2A25-PMD. Figure 1a–e represent the PDFs of RF1, RF2,
204 TB_{3.7}, TB_{10.8} and TB_{12.0} in the 1B01 and 1B01-2A25-PMD, respectively.



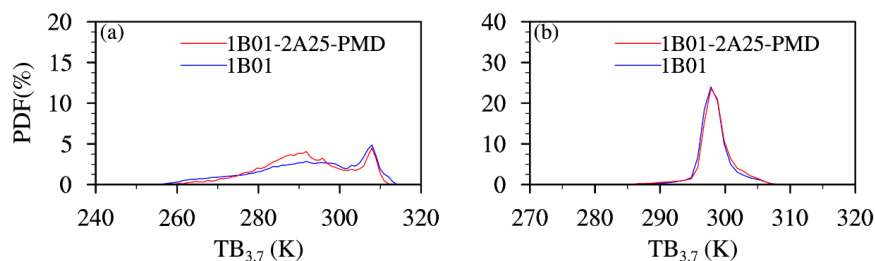
205

206 **Figure 1: PDFs of (a) RF1, (b) RF2, (c) TB_{3.7}, (d) TB_{10.8} and (e) TB_{12.0} in the 1B01 (blue line) and 1B01-2A25-**
207 **PMD (red line) in orbit number 37362 on 5 June 2004.**

208 Figure 1a and 1b show that there is no clear change in RF1 and RF2 after merging. The shape of the
209 PDFs are nearly the same in the 1B01-2A25-PMD and 1B01, with the reflectivity ranging from 0.05 to
210 1.05, but concentrate in the range 0.05–0.3. By contrast, there is a clear variation in TB_{3.7} after merging
211 (Fig. 1c). The PDF of the 1B01 is a single peak with a maximum at 300 K and a sub-peak at 290 K. The
212 PDF of the 1B01-2A25-PMD shows a multi-peak shape, with the peaks mostly in range 280–300 K.
213 TB_{3.7} ranges from 250 to 320 K in both the 1B01 and 1B01-2A25-PMD. The difference in TB_{3.7} between
214 the 1B01 and 1B01-2A25-PMD is probably caused by the uneven cloud distribution. TB_{10.8} and TB_{12.0}
215 have the same distribution after merging. The signals vary from 240 to 300 K and the maxima of the
216 PDFs are both at about 290 K. Although the PDFs of the original and merged datasets are similar, there
217 are slight differences in the peak values. The PDFs of the 1B01-2A25-PMD show lower peaks as a result



218 of data averaging inside the grid (Fig. 1c and 1d).
219 Two regions are selected to analyze the distinctive changes in $TB_{3.7}$ after merging onto the PR pixels: (1)
220 a region that mainly contains cloudy pixels (the cloudy region), and (2) a region that mainly contains
221 clear sky pixels (the clear sky region). When the radiance brightness temperature is greater than 290 K,
222 the pixel is classified as a clear sky pixel, whereas cloudy pixels are classified as those pixels in which
223 the near-surface rain rate is greater than 0.4 mm h^{-1} .

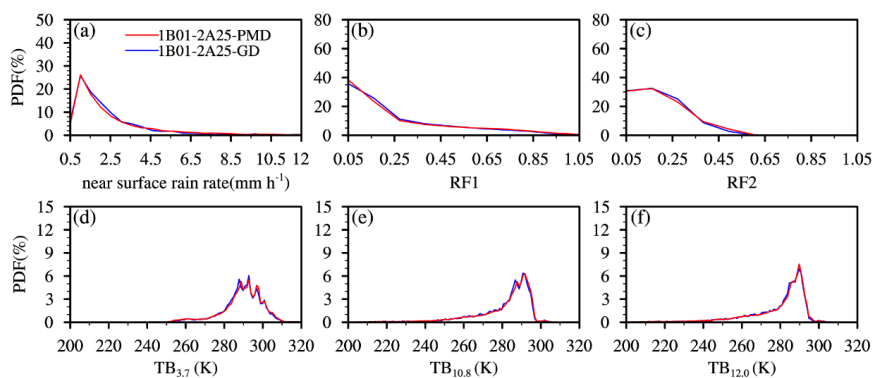


224
225 **Figure 2: PDFs of $TB_{3.7}$ in (a) cloudy regions and (b) clear sky regions in the 1B01 (blue line) and 1B01-2A25-**
226 **PMD (red line) in orbit number 37362 on 5 June 2004.**

227 Fig. 2 shows the PDFs of $TB_{3.7}$ in these two regions. $TB_{3.7}$ ranges from 260 to 315 K in the cloudy region
228 and the maximum value (310 K) is almost the same in both the 1B01 and 1B01-2A25-PMD datasets (Fig.
229 2a). This similarity is also seen in the PDF of $TB_{3.7}$ in the clear sky region, where $TB_{3.7}$ varies between
230 290 and 310 K with a single-peak structure and a maximum at 300 K (Fig. 2b). In a word, the merging
231 process between the PR and the VIRS pixels is considered lead to no dramatic variations on the original
232 data.

233 3.2 Evaluation of the 1B01-2A25-GD

234 The 1B01-2A25-PMD was gridded to match the ERA5 reanalysis data spatially and this dataset is
235 referred to as the 1B01-2A25-Gridded Data (1B01-2A25-GD). Data processing studies have shown that
236 the precision of the spatial resolution of a dataset can affect the accuracy and physical characteristics of
237 the data (Heng and Fu, 2014) and therefore it is essential to evaluate the effects of the gridding process.
238 As an example, Figure 3 compares the near-surface rain rate and the CH1–CH5 signals of the original
239 and gridded data for orbit 37362 on 5 June 2004 in both the 1B01-2A25-PMD and 1B01-2A25-GD.



240
 241 **Figure 3: PDFs of (a) the near-surface rain rate, (b) RF1, (c) RF2, (d) $TB_{3.7}$, (e) $TB_{10.8}$ and (f) $TB_{12.0}$ in the**
 242 **1B01-2A25-PMD (red line) and 1B01-2A25-GD (blue line) in orbit number 37362 on 5 June 2004.**

243 Figure 3a shows that the PDF of the near-surface rain rate in the 1B01-2A25-PMD has a single peak and
 244 the rain rate mainly ranges from 1 to 3 mm h^{-1} . The PDF of the gridded data is nearly the same as that
 245 of the original data, so gridding has little influence on the near-surface rain rate. The PDFs for RF1 and
 246 RF2 are also largely unchanged. RF1 varies from 0.05 to 1.05 and RF2 is mainly in the range 0.05–0.55
 247 (Fig. 3b, 3c). The brightness temperature ($TB_{3.7}$, $TB_{10.8}$ and $TB_{12.0}$) ranges from 240 to 310 K and there
 248 is little difference in the PDFs of the 1B01-2A25-PMD and 1B01-2A25-GD. The PDF of $TB_{3.7}$ has a
 249 multi-peak structure, whereas the PDFs of $TB_{10.8}$ and $TB_{12.0}$ are both single peaks (Fig. 3d–3f). Gridding
 250 therefore does not result in dramatic variations of the parameters in the 1B01-2A25-PMD.

251 Statistical calculations were carried out to quantify the influence of gridding on the 1B01-2A25-PMD.
 252 Table 1 shows the mean, standard deviation (STD) and the corresponding differences of the near-surface
 253 rain rate and the signals from the five channels in the 1B01-2A25-PMD and 1B01-2A25-GD for orbit
 254 37362 on 5 June 2004.

255 **Table 1. Comparisons of statistical mean and standard deviation (STD) of the near-surface rain rate and**
 256 **signals from five channels in the 1B01-2A25-PMD and 1B01-2A25-GD for orbit number 37362 on 5 June 2004.**

	Before gridding		After gridding		Difference	
	Mean	STD	Mean	STD	Mean	STD
RF1	0.112	0.195	0.110	0.189	0.002	0.006
RF2	0.083	0.126	0.082	0.123	0.001	0.003

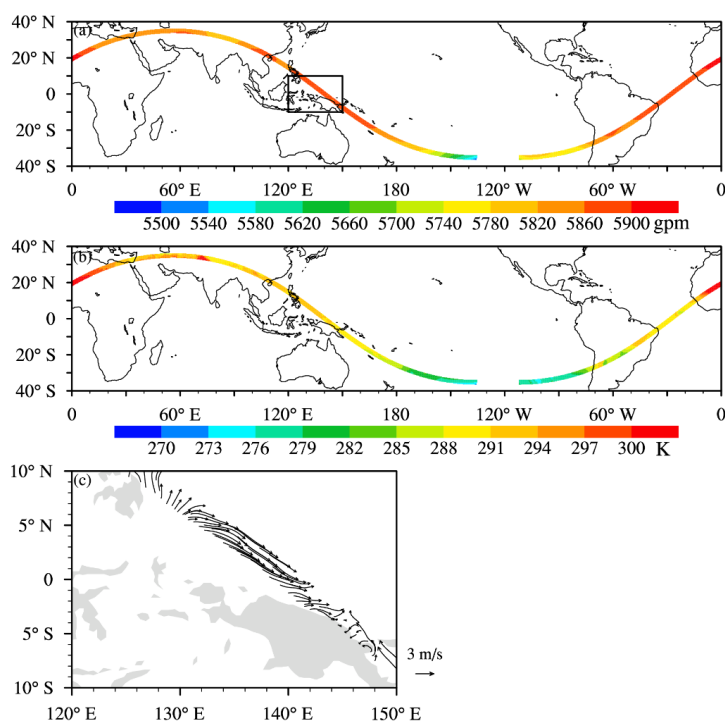


TB _{3,7}	288.805	11.928	288.682	10.631	0.123	1.297
TB _{10,8}	280.516	16.120	280.521	15.397	-0.005	0.723
TB _{12,0}	278.584	16.574	278.628	15.882	-0.044	0.692
Near-surface	3.072	5.121	2.209	2.745	0.861	2.376
rain rate						

257 These results show that the difference in the mean value in this orbit is no more than 0.87 and the STD
258 is no more than 2.38. The differences in the near-surface rain rate are always larger than the differences
259 in the signals for the five channels, although all the differences are acceptable. The statistical results
260 quantitatively verify that the slight influence caused by gridding can be neglected and the parameters in
261 the 1B01-2A25-GD are reliable.

262 3.3 Evaluation of the M-1B01-2A25-GD

263 The ERA5 atmospheric parameters are merged with the 1B01-2A25-GD to establish a new gridded
264 dataset (M-1B01-2A25-GD). The merging process among the 1B01, 2A25 and ERA5 datasets is based
265 on the 2A25, so the detection field is about the same as that measured by the TRMM PR in the new
266 merged dataset. Taking orbit 37362 on 5 June 2004 in the M-1B01-2A25-GD as an example.



267
268 **Figure 4: Distribution of (a) the geopotential height at 500 hPa, (b) the temperature at 850 hPa and (c) the**
269 **wind field at 1000 hPa in orbit number 37362 on 5 June 2004 in the M-1B01-2A25-GD.**

270 Figure 4 shows the geopotential height at 500 hPa, the temperature at 850 hPa and the wind field at 1000
271 hPa. The geopotential height is mainly in the range 5540–5900 gpm and the temperature ranges from
272 270 to 300 K (Fig. 4a, 4b). The box in Fig. 4a shows an enlarged view of the wind field. A strong
273 northwesterly wind appears on the sea surface. The parameters for precipitation, clouds and the
274 atmospheric status provided by the M-1B01-2A25-GD can therefore be used to study the properties of
275 precipitation and clouds systems.

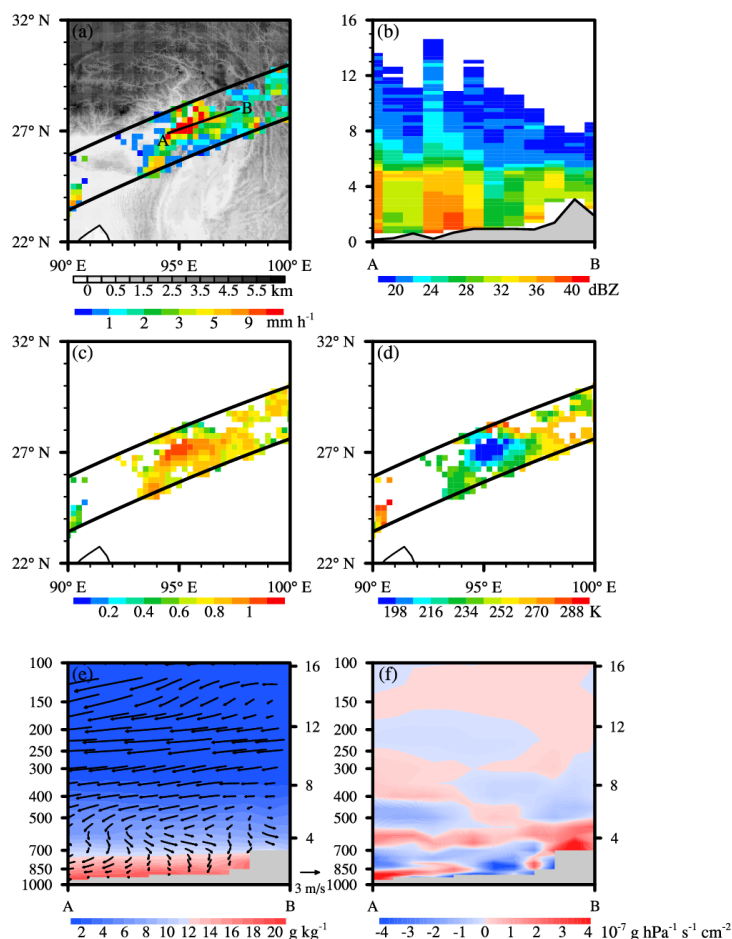
276 **3.4 Applications of the M-1B01-2A25-GD**

277 Evaluations of the M-1B01-2A25-GD show that the merging process does not seriously distort the
278 original data. The new dataset can therefore be used to analyze different types of precipitation and clouds
279 systems. To illustrate the applicability of this new dataset to a variety of different scenarios, we selected
280 precipitation on the trumpet-shaped topography of the Tibetan Plateau, typhoon Rananim precipitation
281 and frontal precipitation in eastern China for further analysis.



282 **3.4.1 Precipitation on the trumpet-shaped topography of the southern Tibetan Plateau**

283 The trumpet-shaped topography of the southern Tibetan Plateau (90°–100° E, 22°–32° N) is the one of
 284 the main channel for the transport of water vapor in this region. The topography here is complex and
 285 there is a clear difference in altitude in the trumpet-shaped area from the hills below the Tibetan
 286 Plateau to the steep slopes and the central Tibetan Plateau. Define these three types of topography as
 287 the foreland under the Tibetan Plateau (FTP), the slope of the trumpet-shaped area (STS) and the
 288 central part of the Tibetan Plateau (CTP).



289
 290 **Figure 5: Case study of precipitation in the trumpet-shaped topography on the Tibetan Plateau on 2 July 2004**
 291 **(orbit number 37786). (a) The near-surface rain rate, (b) vertical cross-sections of the precipitation reflectivity**
 292 **factor, (c) RFI, (d) TB_{10.8}, vertical cross-sections of (e) the wind vectors and specific humidity and (f) the**
 293 **divergence of water vapor flux along line A-B in panel (a).**



294 The precipitation occurred on 2 July 2004 (orbit number 37786). Intense rainfall mainly occurs on the
295 STS with a maximum precipitation intensity over 13 mm h^{-1} . Fig. 5a shows the near-surface rain rate in
296 the rain belt and Fig. 5b shows the vertical cross-section of the precipitation reflectivity factor in the
297 direction of the heavy rainfall center shown in Fig. 5a (line A–B). The altitude varies by 2 km from A to
298 B. The storm top height (STH) refers to the height at which the precipitation reflectivity factor of the
299 three continuous layers is greater than 16 dBZ in the precipitation profiles, decreases gradually and the
300 strong reflectivity factor weakens over the CTP. The intensity of precipitation on the STS from the
301 atmosphere to the land surface first increases and then decreases. There is usually a strong precipitation
302 reflectivity factor 3 km above the land surface. However, the intensity of precipitation on CTP is weaker
303 than that in the FTP. Fu et al. (2017) showed that the elevation of water vapor by the complex topography
304 leads to precipitation on the STS. However, the intensity of precipitation is weak because the water vapor
305 column on the CTP is inadequate due to earlier precipitation on the STS.

306 The physical characteristics of the precipitating clouds are different as a result of the differences in the
307 intensity of precipitation. Fig. 5c shows RF1, which ranges between 0.5 and 1.0, with high values in the
308 areas where precipitation is heavy. A high value of RF1 means there are mainly small particles near the
309 top of the precipitation clouds. $TB_{10.8}$ varies from 190 to 210 K in the region of intense precipitation,
310 which shows that the cloud-top is high. The cloud-top is slightly lower around the precipitating cloud
311 where $TB_{10.8}$ is high (Fig. 5d). In addition to the topographic elevation of water vapor, it is also necessary
312 to understand the status of the atmosphere, including the wind field and water vapor conditions.

313 There is a wet band below 700 hPa with a specific humidity over 15 g kg^{-1} . The specific humidity
314 decreases in the lower layers of the atmosphere from the FTP to the STS and extending to the CTP. A
315 northeasterly airflow prevails below 700 hPa from the CTP via the STS to the FTP. Between 700 and
316 500 hPa, this northeasterly airflow turns to the northwest over the CTP. Above 500 hPa, the airflow is
317 mainly westerly with a higher speed. The water vapor content becomes less favorable for precipitation
318 in the higher atmospheric layers (Fig. 5e). The better water vapor conditions in the lower atmosphere are
319 important for the precipitation process. The upward airflow toward the CTP brings abundant water vapor
320 from the FTP via the STS to the CTP.

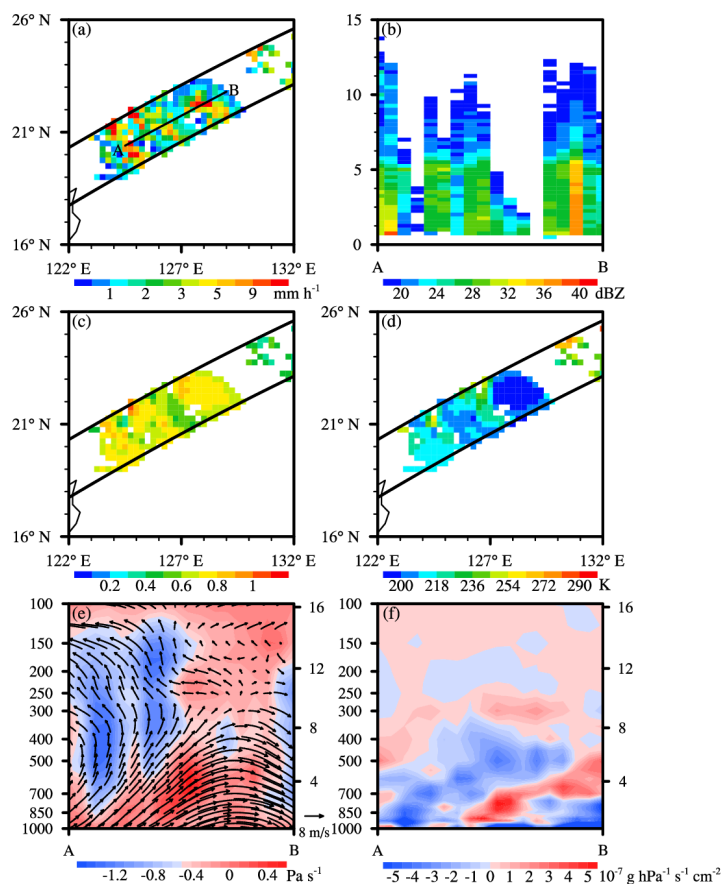
321 The water vapor flux divergence (WVFD) is an important parameter used to describe the status of water
322 vapor transportation in the atmosphere. The WVFD of the FTP is about $1\text{--}3 \times 10^{-7} \text{ g hPa}^{-1} \text{ s}^{-1} \text{ cm}^{-2}$, which



323 means that the water vapor is diverging. The divergence belt extends to the front of the STS. The WVFD
 324 changes to positive on the STS (from -2×10^{-7} to $0 \text{ g hPa}^{-1} \text{ s}^{-1} \text{ cm}^{-2}$), so the water vapor here is in a
 325 convergence field. There is strong divergence on the CTP with a maximum more than $4 \times 10^{-7} \text{ g hPa}^{-1} \text{ s}^{-1}$
 326 cm^{-2} . Fig. 5f shows the complex water vapor transportation processes from the FTP to the CTP. Most of
 327 the transport and exchange of water vapor occurs in the lower atmosphere. There is more water vapor in
 328 the FTP and STS than in the CTP and the intensity of precipitation is heavy in the STS. The elevated
 329 topography increases the transportation of water vapor and chance of precipitation, the wind speed and
 330 convergence of water vapor indeed favor heavy rainfall over the STS.

331 3.4.2 Typhoon Ranim precipitation

332 Second precipitation example, Typhoon Ranim, occurred in the western Pacific (16° – 26° N, 122° – 132°
 333 E) at orbit 38395 on 10 August 2004.



334



335 **Figure 6: Case study of Typhoon Ranim precipitation on 10 August 2004 (orbit number 38395).** (a) The
336 near-surface rain rate, (b) vertical cross-sections of the precipitation reflectivity factor, (c) RF1, (d) TB_{10.8},
337 vertical cross-sections of (e) the wind vectors and vertical velocity and (f) the divergence of water vapor flux
338 along line A-B in panel (a).

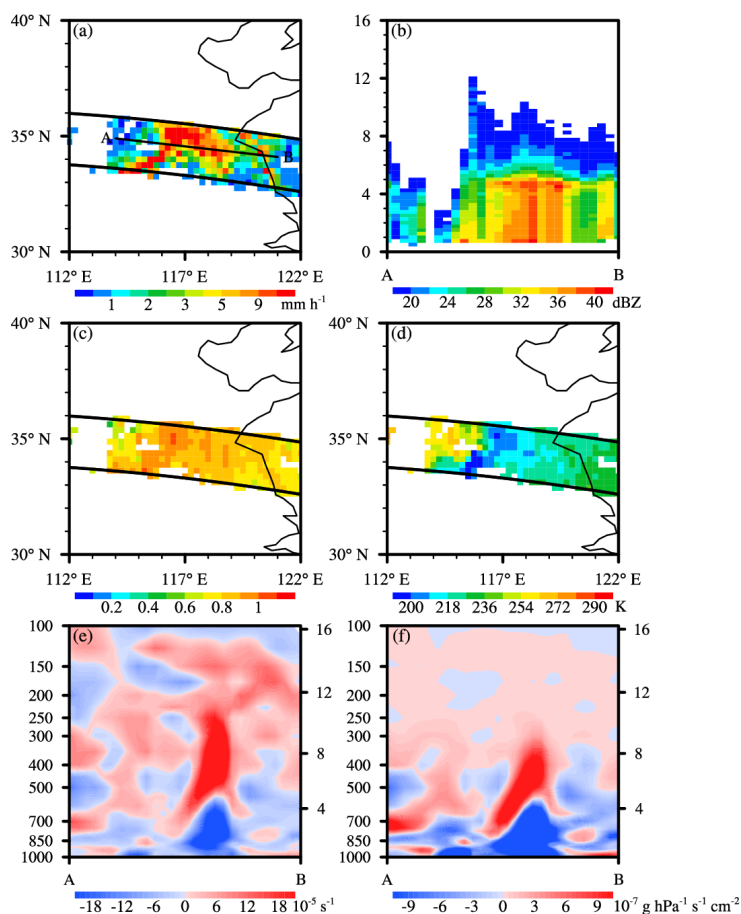
339 The eye of a typhoon is an important indicator over the whole lifetime of the typhoon. The eye of the
340 typhoon shown in Fig. 6a means the typhoon is on the mature stage and the cross-section along line A–
341 B crosses the middle of the eye. The STH is higher than 13 km in the eye wall region, which means that
342 strong convection occurs here, but is lower than 5 km in the eye of the typhoon. The maximum
343 precipitation reflectivity factor exceeds 35 dBZ, but the precipitation intensity inside the eye is weak,
344 resulting in a low precipitation reflectivity factor and STH (Fig. 6b).

345 RF1 varies from 0.5 to 1. The particles near the precipitating cloud-top are small near the eye wall, which
346 leads to strong scatter in the visible spectrum (Fig. 6c). The distribution of TB_{10.8} shows the height of the
347 precipitating cloud-top, which also indirectly represents convection inside the precipitation system.
348 TB_{10.8} is less than 235 K around the eye of the typhoon. A low brightness temperature means a high
349 precipitating cloud-top. The STH is low and the cloud-top is high in some regions as a result of cirrus
350 clouds (Fig. 6d). The maximum descending speed in the typhoon eye is over 0.5 Pa s⁻¹ and a
351 southwesterly airflow prevails at high speeds below 400 hPa. The airflow is in the opposite direction at
352 low speeds above 400 hPa. The maximum ascending speed in the eye wall reaches -1.5 Pa s⁻¹ (Fig. 6e).

353 Figure 6f shows the transportation of water vapor in the typhoon system along line A–B. There is strong
354 convergence of water vapor below 700 hPa and the maximum WVFD is $-5 \times 10^{-7} \text{ g hPa}^{-1} \text{ s}^{-1} \text{ cm}^{-2}$. There
355 exists a belt of divergence in the middle of the convergence field with WVFD values ranging from 2×10^{-7}
356 to $5 \times 10^{-7} \text{ g hPa}^{-1} \text{ s}^{-1} \text{ cm}^{-2}$. Water vapor is usually transported in the lower layers of the atmosphere.
357 Water vapor is exchanged between the typhoon and the eye wall, so the intensity of precipitation is
358 different at various locations in the typhoon system.

359 **3.4.2 Frontal precipitation in eastern China**

360 In frontal systems, precipitation is induced by the elevation of air masses when two types of air flow
361 meet. As an example, frontal precipitation case that occurred in eastern China (30°–40° N, 112°–122° E)
362 on 22 June 2003 at orbit 31926 is analyzed.



363

364 **Figure 7: Case study of frontal precipitation on 3 June 2003 (orbit number 31926). (a) The near-surface rain**
365 **rate, vertical cross-sections of (b) the precipitation reflectivity factor, (c) RF1, (d) $TB_{10.8}$, vertical cross-sections**
366 **of (e) divergence and (f) the divergence of water vapor flux along line A-B in panel (a).**

367 Fig. 7a clearly shows the rain belt at the boundary of the different airflows. The maximum precipitation
368 intensity is more than 10 mm h^{-1} . Fig. 7b shows the precipitation reflectivity factor profiles of line A–B
369 to illustrate the vertical structure. The reflectivity factor is high from the land surface to 5 km and the
370 maximum exceeds 42 dBZ. The size of precipitating cloud droplets in the heavy rainfall system is usually
371 small near the precipitating cloud-top, as shown by RF1 values bigger than 0.8 (Fig. 7c). $TB_{10.8}$ varies
372 between 200 and 235 K in the area of strong precipitation intensity and the minimum appears in the front,
373 where the height of the precipitating cloud-top is highest. The difference in the brightness temperature
374 on each side of the front represents the difference in the height of the precipitating cloud-top (Fig. 7d).



375 Figure 7e shows that the calculated divergence in the cross-section, which represents convergence below
376 700 hPa, reaches $-18 \times 10^{-5} \text{ s}^{-1}$. Strong divergence over $18 \times 10^{-5} \text{ s}^{-1}$ occurs above 500 hPa. The WVFD
377 has the same distribution as the divergence. The maximum WVFD exceeds $-10 \times 10^{-7} \text{ g hPa}^{-1} \text{ s}^{-1} \text{ cm}^{-2}$
378 below 700 hPa. Strong divergence of the water vapor occurs above 500 hPa, with a WVDF of $9 \times 10^{-7} \text{ g}$
379 $\text{hPa}^{-1} \text{ s}^{-1} \text{ cm}^{-2}$. The exchange of water vapor often occurs below 200 hPa (Fig. 6f). The atmospheric
380 status satisfies the precipitation condition and shows the complexity of vertical motion in the atmosphere.

381 4 Discussion

382 Due to the rapid development of the technology of satellite and emergence of the various satellite data
383 products. Huge amount of the satellite datasets usually leads to difficulty in data storage. The M-1B01-
384 2A25-GD is a grid-level dataset with spatial resolution of 0.25° which can largely reduce the digital
385 storage space required. This new dataset will become a demonstration for satellite data processing.

386 The data merging among the precipitation parameters (profiles of rain rate and precipitation reflectivity
387 factor, near-surface rain rate and rain type) measured by the PR, spectral signals measured by the VIRS
388 and atmospheric parameters (temperature, specific humidity, wind field, geopotential height, divergence
389 and vertical velocity) of the ERA5 reanalysis dataset is an initial attempt. This dataset can be helpful in
390 studying the characteristics and changes in precipitation and the clouds systems. To further explore the
391 relationship among the precipitation, clouds and atmospheric parameters, the cloud parameters based on
392 the signals retrieval from the TRMM VIRS data will be added to the merged dataset. The work is now in
393 progress and will not be involved in this study due to the limited length of the paper.

394 The studies on the atmospheric dynamics and cloud physics are isolated because of the lack of the suitable
395 datasets. Now, the problem can be solved through establishing the new merged dataset. The
396 comprehensive parameters about precipitation, clouds and atmosphere can be obtained in each single
397 orbit from the M-1B01-2A25-GD to support the case analysis and model simulations.

398 5 Data availability

399 The used M-1B01-2A25-GD in this paper are accessible at <http://doi.org/10.5281/zenodo.4458868> (Sun
400 and Fu, 2021).



401 **6 Conclusions**

402 We establish a new merged gridded dataset M-1B01-2A25-GD combining satellite and reanalysis
403 datasets. The precipitation, cloud and atmospheric parameters are spatially and temporally collocated.
404 The gridded data helps to reduce the digital storage space required. The statistical results show that there
405 is no obvious bias in the 1B01-2A25-PMD when compared with the original swath-level data measured
406 by the TRMM VIRS. The 1B01-2A25-GD has the same spatial resolution as the ERA5 reanalysis dataset.
407 The average inside the grid leads to smoothing effects on the maximum and minimum values, but does
408 not adversely influence the parameters in the 1B01-2A25-PMD. The difference in the mean value is no
409 more than 0.87 and the STD is no more than 2.38 for the near-surface rain rate and signals measured by
410 the VIRS over one orbit. The M-1B01-2A25-GD contains comprehensive parameters about precipitation,
411 clouds and the atmosphere that are useful in studies of the characteristics and distribution of precipitation
412 and clouds systems in the tropics and subtropics. Three typical applications of the M-1B01-2A25-GD
413 are introduced by analyzing different examples of precipitation. This new dataset can support studies of
414 precipitation, clouds systems and model simulations. Longer time periods of data and more parameters
415 will be added as satellite technology and models are improved.

416 **Author contribution.** Lilu Sun and Yunfei Fu prepared the data in the standardized format. Lilu Sun
417 uploaded the data in the data repository and prepared the manuscript with contributions from all co-
418 authors.

419 **Competing interests.** The authors declare that they have no conflict of interests.

420 **Financial support.** This research was supported by the
421 National Natural Science Foundation of China (Grants 91837310, 41675041).

422 **References**

423 Awaka, J., Iguchi, T., Kumagai, H., and Okamoto, K.: Rain type classification algorithm for TRMM
424 precipitation radar, IEEE International Geoscience and Remote Sensing Symposium Proceedings.
425 Remote Sensing - A Scientific Vision for Sustainable Development, Singapore, 3-8 August 1997,



- 426 <https://doi.org/10.1109/IGARSS.1997.608993>, 1997.
- 427 Baker, M. B.: Cloud Microphysics and Climate, *Science*, 276, 1072-1078,
428 <https://doi.org/10.1126/science.276.5315.1072>, 1997.
- 429 Chen, F., and Fu, Y. F.: Characteristics of typhoon precipitation and non-typhoon precipitation over East
430 Asia based on merged PR and VIRS data, *Climatic. Environ. Res.* (in Chinese), 20, 62-74,
431 <https://doi.org/10.3878/j.issn.1006-9585.2014.14031>, 2015.
- 432 Chen, F., Sheng, S., Bao, Z., Wen, H., Hua, L., Paul, N. J., and Fu, Y.: Precipitation Clouds Delineation
433 Scheme in Tropical Cyclones and Its Validation Using Precipitation and Cloud Parameter Datasets from
434 TRMM, *J. Appl. Meteorol. Climatol.*, 57, 821-836, <https://doi.org/10.1175/jamc-d-17-0157.1>, 2018.
- 435 Chen, Y., and Fu, Y.: Characteristics of VIRS Signals within Pixels of TRMM PR for Warm Rain in the
436 Tropics and Subtropics, *J. Appl. Meteorol. Climatol.*, 56, 789-801, <https://doi.org/10.1175/jamc-d-16-0198.1>, 2017.
- 438 Durden, S. L., Im, E., Haddad, Z. S., and Li, L.: Comparison of TRMM precipitation radar and airbone
439 radar data, *J. Appl. Meteorol.*, 42, 769-774, [https://doi.org/10.1175/1520-0450\(2003\)0422.0.CO;2](https://doi.org/10.1175/1520-0450(2003)0422.0.CO;2), 2003.
- 440 Fu, Y. F. and Liu, G. S.: The variability of tropical precipitation profiles and its impact on microwave
441 brightness temperatures as inferred from TRMM data, *J. Appl. Meteorol.*, 40, 2130-2143,
442 [https://doi.org/10.1175/1520-0450\(2001\)0402.0.CO;2](https://doi.org/10.1175/1520-0450(2001)0402.0.CO;2), 2001.
- 443 Fu, Y., Liu, G., Wu, G., Yu, R., Xu, Y., Wang, Y., Li, R., and Liu, Q.: Tower mast of precipitation over
444 the central Tibetan Plateau summer, *Geophys. Res. Lett.*, 33, <https://doi.org/10.1029/2005gl024713>,
445 2006.
- 446 Fu, Y., Liu, Q., Gao, Y., Hong, X., Zi, Y., Zheng, Y., Li, R., and Heng, Z.: A feasible method for merging
447 the TRMM microwave imager and precipitation radar data, *J. Quant. Spectrosc. Ra.*, 122, 155-169,
448 <https://doi.org/10.1016/j.jqsrt.2012.08.028>, 2013.
- 449 Fu, Y., Pan, X., Xian, T., Liu, G., Zhong, L., Liu, Q., Li, R., Wang, Y., and Ma, M.: Precipitation
450 characteristics over the steep slope of the Himalayas in rainy season observed by TRMM PR and VIRS,
451 *Clim. Dynam.*, 51, 1971-1989, <https://doi.org/10.1007/s00382-017-3992-3>, 2017.
- 452 Fu, Y., and Zhang, A.: Life Cycle Effects on the Vertical Structure of Precipitation in East China
453 Measured by Himawari-8 and GPM DPR, *Mon. Weather. Rev.*, 146, 2183-2199,
454 <https://doi.org/10.1175/mwr-d-18-0085.1>, 2018.



- 455 Fu, Y. F., Liu, Q., Zi, Y., Feng, S., Li, Y., and Liu, G. S.: Summer Precipitation and Latent Heating over
456 the Tibet Plateau Based on TRMM Measurements, *Plateau. Mountain. Meteor. Res.* (in Chinese), 28, 8-
457 18, <https://doi.org/10.3969/j.issn.1674-2184.2008.01.002>, 2008.
- 458 Fu, Y. F., Liu, P., Liu, Q., Ma, M., Sun, L., and Wang, Y.: Climatological Characteristics of VIRS
459 Channels for Precipitating Cloud in Summer Over the Tropics and Subtropics, *Journal of Atmospheric
460 and Environmental Optics* (in Chinese), 6, 129-140, [https://doi.org/10.3969/j.issn.1673-
461 6141.2011.02.009](https://doi.org/10.3969/j.issn.1673-6141.2011.02.009), 2011.
- 462 Fu, Y. F.: Cloud Parameters retrieved by the bispectral reflectance algorithm and associated applications,
463 *J. Meteorol. Res.-Proc.*, 28, 965-982, <https://doi.org/CNKI:SUN:QXXW.0.2014-05-019>, 2014.
- 464 Gao, W., Liu, L., Li, J., and Lu, C.: The Microphysical Properties of Convective Precipitation Over the
465 Tibetan Plateau by a Subkilometer Resolution Cloud-Resolving Simulation, *J. Geophys. Res.-Atmos.*,
466 123, 3212-3227, <https://doi.org/10.1002/2017jd027812>, 2018.
- 467 Hartmann, D. L., and Short, D. A.: On the Use of Earth Radiation Budget Statistics for Studies of Clouds
468 and Climate, *J. Atmos. Sci.*, 37, 1233-1250, [https://doi.org/10.1175/1520-
469 0469\(1980\)037<1233:Otuoe>2.0.Co;2](https://doi.org/10.1175/1520-0469(1980)037<1233:Otuoe>2.0.Co;2), 1980.
- 470 Hawkins, J., Miller, S., Mitrescu, C., L'Ecuyer, T., Turk, J., Partain, P., and Stephens, G.: Near-Real-Time
471 Applications of CloudSat Data, *J. Appl. Meteorol. Climatol.*, 47, 1982-1994,
472 <https://doi.org/10.1175/2007jamc1794.1>, 2008.
- 473 Hayasaka, T., Kozu, T., Iguchi, T., Meneghini, R., Awaka, J., Okamoto, K. i., Wu, D. L., Jin, Y., and Jiang,
474 J.: Preliminary test results of a rain rate profiling algorithm for the TRMM precipitation radar, *Microwave
475 Remote Sensing of the Atmosphere and Environment, China*, 19 August 1998,
476 <https://doi.org/10.1117/12.319497>, 1998.
- 477 Heng, Z., and Fu, Y. F.: Impact of gridding scale on TRMM microwave imager cloud water information,
478 *Climatic. Environ. Res.* (in Chinese), 19, 693-702, <https://doi.org/10.3878/j.issn.1006-9585.2013.13049>,
479 2014.
- 480 Hersbach, H., Bell, B., Berrisford, P., Hirahara, S., Horányi, A., Muñoz-Sabater, J., Nicolas, J., Peubey,
481 C., Radu, R., Schepers, D., Simmons, A., Soci, C., Abdalla, S., Abellan, X., Balsamo, G., Bechtold, P.,
482 Biavati, G., Bidlot, J., Bonavita, M., Chiara, G., Dahlgren, P., Dee, D., Diamantakis, M., Dragani, R.,
483 Flemming, J., Forbes, R., Fuentes, M., Geer, A., Haimberger, L., Healy, S., Hogan, R. J., Hólm, E.,



484 Janisková, M., Keeley, S., Laloyaux, P., Lopez, P., Lupu, C., Radnoti, G., Rosnay, P., Rozum, I., Vamborg,
485 F., Villaume, S., and Thépaut, J. N.: The ERA5 global reanalysis, *Q. J. R. Meteorol. Soc.*, 146, 1999-
486 2049, <https://doi.org/10.1002/qj.3803>, 2020.

487 Hobbs, P. V.: Research on the clouds and precipitation past present and future, Part II, *Bull. Am. Meteorol.*
488 *Soc.*, 72, 184-191, [https://doi.org/10.1175/1520-0477\(1991\)072<0184:ROCAPP>2.0.CO;2](https://doi.org/10.1175/1520-0477(1991)072<0184:ROCAPP>2.0.CO;2), 1991.

489 Houze, R. A.: Structures of atmospheric precipitation systems A global survey, *Radio. Sci.*, 16, 671-689,
490 <https://doi.org/10.1029/RS016i005p00671>, 1981.

491 Houze, R. A.: Stratiform Precipitation in Regions of Convection: A Meteorological Paradox?, *Bull. Am.*
492 *Meteorol. Soc.*, 78, 2179-2196, [https://doi.org/10.1175/1520-0477\(1997\)078<2179:SPIROC>2.0.CO;2](https://doi.org/10.1175/1520-0477(1997)078<2179:SPIROC>2.0.CO;2),
493 1997.

494 Iguchi, T., Meneghini, R., Awaka, J., Kozu, T., and Okamoto, K.: Rain profiling algorithm for TRMM
495 Precipitation Radar data, *Adv. Space. Res.*, 25, 973-976, [https://doi.org/10.1016/S0273-1177\(99\)00933-](https://doi.org/10.1016/S0273-1177(99)00933-3)
496 3, 2000.

497 Kienast-Sjögren, E., Rolf, C., Seifert, P., Krieger, U. K., Luo, B. P., Krämer, M., and Peter, T.:
498 Climatological and radiative properties of midlatitude cirrus clouds derived by automatic evaluation of
499 lidar measurements, *Atmos. Chem. Phys.*, 16, 7605-7621, <https://doi.org/10.5194/acp-16-7605-2016>,
500 2016.

501 Kozu, T., Kawanishi, T., Kuroiwa, H., Oikawa, M., Kumagai, H., Okamoto, K., Okumura, M., Nakatsuka,
502 H., and Nishikawa, K.: Development of precipitation radar onboard the Tropical Rainfall Measuring
503 Mission (TRMM) satellite., *IEEE. Trans. Geosci. Remote. Sens.*, 39, 102-116,
504 <https://doi.org/10.1109/36.898669>, 2001.

505 Kummerow, C., William, S., and Giglio, L.: A simplified scheme for obtaining precipitation and vertical
506 hydrometeor profiles from passive microwave sensors, *IEEE. Trans. Geosci. Remote. Sens.*, 34, 1213-
507 1232, <https://doi.org/10.1109/36.536538>, 1996.

508 Kummerow, C., Barnes, W., Kozu, T., Shiue, J., and Simpson, J.: The tropical rainfall measuring mission
509 (TRMM) sensor package, *J. Atmos. Ocean. Tech.*, 15, 809-817, [https://doi.org/10.1175/1520-](https://doi.org/10.1175/1520-0426(1998)015<0809:TTRMMT>2.0.CO;2)
510 0426(1998)015<0809:TTRMMT>2.0.CO;2, 1998.

511 Kummerow, C., Simpson, J., Thiele, O., Barnes, W., Chang, A. T. C., Stocker, E., Adler, R. F., Hou, A.,
512 Kakar, R., Wentz, F., Ashcroft, P., Kozu, T., Hong, Y., Okamoto, K., Iguchi, T., Kuroiwa, H., Im, E.,



- 513 Haddad, Z., Huffman, G., Ferrier, B., Olson, W. S., Zipser, E., Smith, E. A., Wilhelm, T. T., North, G.,
514 Krishnamurti, T., and Nakamura, K.: The status of the TRMM after two years in orbit, *J. Appl. Meteorol.*
515 *Climatol.*, 39, 1965-1982, [https://doi.org/10.1175/1520-0450\(2001\)040<1965:TSOTTR>2.0.CO;2](https://doi.org/10.1175/1520-0450(2001)040<1965:TSOTTR>2.0.CO;2),
516 2000.
- 517 Lau, K. M., and Wu, H. T.: Characteristics of Precipitation, Cloud, and Latent Heating Associated with
518 the Madden-Julian Oscillation, *J. Climate.*, 23, 504-518, <https://doi.org/10.1175/2009jcli2920.1>, 2010.
- 519 Li, J., Lv, Q., Jian, B., Zhang, M., Zhao, C., Fu, Q., Kawamoto, K., and Zhang, H.: The impact of
520 atmospheric stability and wind shear on vertical cloud overlap over the Tibetan Plateau, *Atmos. Chem.*
521 *Phys.*, 18, 7329-7343, <https://doi.org/10.5194/acp-18-7329-2018>, 2018.
- 522 Li, R., and Fu, Y. F.: Tropical Precipitation Estimated by GPCP and TRMM PR Observations, *Adv. Atmos.*
523 *Sci.*, 22, 852-864, <https://doi.org/10.1007/BF02918685>, 2005.
- 524 Liou, K.-N.: Influence of Cirrus Clouds on Weather and Climate Processes: A Global Perspective, *Mon.*
525 *Weather. Rev.*, 114, 1167-1199, [https://doi.org/10.1175/1520-0493\(1986\)114<1167:Ioccow>2.0.Co;2](https://doi.org/10.1175/1520-0493(1986)114<1167:Ioccow>2.0.Co;2),
526 1986.
- 527 Liu, C., and Zipser, E. J.: "Warm Rain" in the Tropics: Seasonal and Regional Distributions Based on 9
528 yr of TRMM Data, *J. Climate.*, 22, 767-779, <https://doi.org/10.1175/2008jcli2641.1>, 2009.
- 529 Liu, G. S., and Fu, Y. F.: The Characteristics of tropical precipitation profiles as inferred from satellite
530 radar measurements, *J. Meteorol. Soc. Jpn.*, 79, 131-143, <https://doi.org/10.2151/jmsj.79.131>, 2001.
- 531 Liu, Q., and Fu, Y. F.: Characteristics of latent heating over the Tibetan Plateau during summer, *Journal*
532 *of University of Science and Technology of China (in Chinese)*, 37, 303-309,
533 <https://doi.org/10.3969/j.issn.0253-2778.2007.03.015>, 2007.
- 534 Liu, Q., and Fu, Y.: Comparison of radiative signals between precipitating and non-precipitating clouds
535 in frontal and typhoon domains over East Asia, *Atmos. Res.*, 96, 436-446,
536 <https://doi.org/10.1016/j.atmosres.2010.02.003>, 2010.
- 537 Lu, D., Yang, Y., and Fu, Y.: Interannual variability of summer monsoon convective and stratiform
538 precipitations in East Asia during 1998-2013, *Int. J. Climatol.*, 36, 3507-3520,
539 <https://doi.org/10.1002/joc.4572>, 2016.
- 540 Luo, S., Fu, Y., Zhou, S., Wang, X., and Wang, D.: Analysis of the Relationship between the Cloud Water
541 Path and Precipitation Intensity of Mature Typhoons in the Northwest Pacific Ocean, *Adv. Atmos. Sci.*,



- 542 37, 359-376, <https://doi.org/10.1007/s00376-020-9204-9>, 2020.
- 543 Luo, Y., Zhang, R., and Wang, H.: Comparing Occurrences and Vertical Structures of Hydrometeors
544 between Eastern China and the Indian Monsoon Region Using CloudSat/CALIPSO Data, *J. Climate.*, 22,
545 1052-1064, <https://doi.org/10.1175/2008jcli2606.1>, 2009.
- 546 Min, Q., Li, R., Wu, X., and Fu, Y.: Retrieving latent heating vertical structure from cloud and
547 precipitation Profiles—Part I: Warm rain processes, *J. Quant. Spectrosc. Ra.*, 122, 31-46,
548 <https://doi.org/10.1016/j.jqsrt.2012.11.030>, 2013.
- 549 Nesbitt, S. W., Zipser, E. J., and Cecil, D. J.: A census of precipitation features in the tropics using TRMM
550 Radar, ice scattering, and lightning observations, *J. Climate.*, 13, 4087-4106,
551 [https://doi.org/10.1175/1520-0442\(2000\)0132.0.CO;2](https://doi.org/10.1175/1520-0442(2000)0132.0.CO;2), 1999.
- 552 Oki, T., and Kanae, S.: Global hydrological cycles and world water resources, *Science*, 313, 1068-1072,
553 <https://doi.org/10.1126/science.1128845>, 2006.
- 554 Olson, W. S., Kummerow, C. D., Heymsfield, G. M., and Giglio, L.: A Method for Combined Passive-
555 Active Microwave Retrievals of Cloud and Precipitation Profiles, *J. Appl. Meteorol.*, 35, 1763-1789,
556 [https://doi.org/10.1175/1520-0450\(1996\)035<1763:Amfcpm>2.0.Co;2](https://doi.org/10.1175/1520-0450(1996)035<1763:Amfcpm>2.0.Co;2), 1996.
- 557 Pan, X., and Fu, Y. F.: Analysis on Climatological Characteristics of Deep and Shallow Precipitation
558 Cloud in Summer over Qinghai-Xizang Plateau, *Plateau. Meteor. (in Chinese)*, 34, 1191-1203,
559 <https://doi.org/10.7522/j.issn.1000-0534.2014.00112>, 2015.
- 560 Petty, G. W.: Physical retrievals of over-ocean rain rate from multichannel microwave imagery. Part I:
561 Theoretical Characteristics of Normalized Polarization and Scattering Indices, *Meteorol. Atmos. Phys.*,
562 54, 79-99, <https://doi.org/10.1007/BF01030054>, 1994.
- 563 Roscow, William, B., and Robert, A.: Advances in understanding clouds from ISCCP, *Bull. Am. Meteorol.*
564 *Soc.*, 80, 2261-2288, [https://doi.org/10.1175/1520-0477\(1999\)080<2261:AIUCFI>2.0.CO;2](https://doi.org/10.1175/1520-0477(1999)080<2261:AIUCFI>2.0.CO;2), 1999.
- 565 Sassen, K., Wang, Z., and Liu, D.: Cirrus clouds and deep convection in the tropics: Insights from
566 CALIPSO and CloudSat, *J. Geophys. Res.*, 114, D00H06, <https://doi.org/10.1029/2009jd011916>, 2009.
- 567 Schumacher, C., and Houze, R. A.: The TRMM precipitation radar's view of shallow, isolated rain, *J.*
568 *Appl. Meteorol.*, 42, 1519-1524, [https://doi.org/10.1175/1520-0450\(2003\)042<1519:TTPRVO>2.0.CO;2](https://doi.org/10.1175/1520-0450(2003)042<1519:TTPRVO>2.0.CO;2), 2003.
- 570 Simpson, J., Kummerow, C., Tao, W.-K., and Adler, R. F.: On the Tropical Rainfall Measuring Mission



- 571 (TRMM), *Meteorol. Atmos. Phys.*, 60, 19-36, <https://doi.org/10.1007/BF01029783>, 1996.
- 572 Sun, L. L., and Fu, Y. F.: A new merged dataset for analyzing clouds, precipitation and atmospheric
573 parameters based on ERA5 reanalysis data and the measurements of TRMM PR and VIRS. Zenodo,
574 <http://doi.org/10.5281/zenodo.4458868>, 2021.
- 575 Szoke, E. J., Zipser, E. J., and Jorgensen, D. P.: A Radar Study of Convective Cells in Mesoscale Systems
576 in GATE. Part I: Vertical Profile Statistics and Comparison with Hurricanes, *J. Atmos. Sci.*, 43, 182-198,
577 [https://doi.org/10.1175/1520-0469\(1986\)043<0182:Arsocc>2.0.Co;2](https://doi.org/10.1175/1520-0469(1986)043<0182:Arsocc>2.0.Co;2), 1986.
- 578 Tustison, B., Foufoula-Georgiou, E., and Harris, D.: Scale-recursive estimation for multisensor
579 Quantitative Precipitation Forecast verification: A preliminary assessment, *J. Geophys. Res.*, 108, CIP2-
580 1-14 <https://doi.org/10.1029/2001jd001073>, 2002.
- 581 Wang, R., and Fu, Y.: Structural characteristics of atmospheric temperature and humidity inside clouds
582 of convective and stratiform precipitation in the rainy season over East Asia, *J. Meteorol. Res-Proc.*, 31,
583 890-905, <https://doi.org/10.1007/s13351-017-7038-x>, 2017.
- 584 Wang, R., Fu, Y., Xian, T., Chen, F., Yuan, R., Li, R., and Liu, G.: Evaluation of Atmospheric Precipitable
585 Water Characteristics and Trends in Mainland China from 1995 to 2012, *J. Climate.*, 30, 8673-8688,
586 <https://doi.org/10.1175/jcli-d-16-0433.1>, 2017.
- 587 Wang, Y., Zhang, Y., Fu, Y., Li, R., and Yang, Y.: A climatological comparison of column-integrated water
588 vapor for the third-generation reanalysis datasets, *Sci. China Earth Sci.*, 59, 296-306,
589 <https://doi.org/10.1007/s11430-015-5183-6>, 2015.
- 590 Wetherald, R. T., and Manabe, S.: Cloud Feedback Processes in a General Circulation Model, *J. Atmos.*
591 *Sci.*, 45, 1397-1416, [https://doi.org/10.1175/1520-0469\(1988\)045<1397:Cfpiag>2.0.Co;2](https://doi.org/10.1175/1520-0469(1988)045<1397:Cfpiag>2.0.Co;2), 1988.
- 592 Wilheit, T. T., Chang, A. T. C., V. Rao, M. S., Rodgers, E. B., and Theon, J. S.: A Satellite Technique for
593 Quantitatively Mapping Rainfall Rates over the Oceans, *J. Appl. Meteorol.*, 16, 551-560,
594 [https://doi.org/10.1175/1520-0450\(1977\)016<0551:Astfqm>2.0.Co;2](https://doi.org/10.1175/1520-0450(1977)016<0551:Astfqm>2.0.Co;2), 1977.
- 595 Xia, J., and Fu, Y. F.: The vertical characteristics of temperature and humidity inside convective and
596 stratiform precipitating clouds in the East Asian summer monsoon region and Indian summer monsoon
597 region, *Chinese. J. Atmos. Sci. (in Chinese)*, 40, 563-580, <https://doi.org/10.3878/j.issn.1006->
598 9895.1507.15123, 2016.
- 599 Yang, Y.-J., Lu, D.-R., Fu, Y.-F., Chen, F.-J., and Wang, Y.: Spectral Characteristics of Tropical Anvils



600 Obtained by Combining TRMM Precipitation Radar with Visible and Infrared Scanner Data, *Pure Appl.*
601 *Geophys.*, 172, 1717-1733, <https://doi.org/10.1007/s00024-014-0965-x>, 2014.

602 Yuter, S. E., and Houze, R. A.: Three-Dimensional Kinematic and Microphysical Evolution of Florida
603 Cumulonimbus. Part III: Vertical Mass Transport, Mass Divergence, and Synthesis, *Mon. Weather. Rev.*,
604 123, 1964-1983, [https://doi.org/10.1175/1520-0493\(1995\)123<1964:TDKAME>2.0.CO;2](https://doi.org/10.1175/1520-0493(1995)123<1964:TDKAME>2.0.CO;2), 1995.

605 Zhao, B., Zhang, B., Shi, C., Liu, J., and Jiang, L.: Comparison of the Global Energy Cycle between
606 Chinese Reanalysis Interim and ECMWF Reanalysis, *J. Meteorol. Res-Prc.*, 33, 563-575,
607 <https://doi.org/10.1007/s13351-019-8129-7>, 2019.

608 Zheng, X. Y., Fu, Y. F., Yang, Y. J., and Liu, G. S.: Impact of atmospheric circulations on aerosol
609 distributions in autumn over eastern China: observational evidence, *Atmos. Chem. Phys.*, 15, 12115-
610 12138, <https://doi.org/10.5194/acp-15-12115-2015>, 2015.

611 Zipser, E. J., and Lutz, K. R.: The Vertical Profile of Radar Reflectivity of Convective Cells: A Strong
612 Indicator of Storm Intensity and Lightning Probability?, *Mon. Weather. Rev.*, 122, 1751-1759,
613 [https://doi.org/10.1175/1520-0493\(1994\)122<1751:Tvporr>2.0.Co;2](https://doi.org/10.1175/1520-0493(1994)122<1751:Tvporr>2.0.Co;2), 1994.

614
615